

Non-centrosymmetric Sr₂IrO₄ obtained under High Pressure

Haozhe Wang^{1‡}, Madalynn Marshall^{2‡}, Zhen Wang³, Kemp W. Plumb⁴, Martha Greenblatt², Yimei Zhu³, David Walker⁵, Weiwei Xie^{1*}

1. Department of Chemistry, Michigan State University, East Lansing, Michigan 48824, USA
2. Department of Chemistry and Chemical Biology, Rutgers University, Piscataway, New Jersey 08854, USA
3. Condensed Matter Physics and Materials Science Department, Brookhaven National Laboratory, Upton, New York 11973, USA
4. Department of Physics, Brown University, Providence, Rhode Island 02912, USA
5. Lamont Doherty Earth Observatory, Columbia University, Palisades, New York 10964, USA

‡ H.W. and M.M. contributed equally. * Email: xieweiwe@msu.edu

Abstract

Sr₂IrO₄ with strong spin-orbit coupling (SOC) and Hubbard repulsion (U) hosts Mott insulating states. The similar crystal structure, magnetic and electronic properties, particularly the *d*-wave gap observed in Sr₂IrO₄ enhanced the analogies to cuprate high-*T_c* superconductor, La₂CuO₄. The incomplete analogy was due to the lack of broken inversion symmetry phases observed in Sr₂IrO₄. Here, under high pressure and high temperature conditions, we report a non-centrosymmetric Sr₂IrO₄. The crystal structure and its noncentrosymmetric character were determined by single crystal X-ray diffraction and high-resolution scanning transmission electron microscopy (HR-STEM). The magnetic characterization confirms the Ir⁴⁺ with *S* = 1/2 at low temperature in Sr₂IrO₄ with magnetic ordering occurred at around 86 K, where a larger moment is observed than the ambient pressure Sr₂IrO₄. Moreover, the resistivity measurement shows three-dimensional Mott variable-range hopping existed in the system. This non-centrosymmetric Sr₂IrO₄ phase appears to be a unique material to offer further understanding of high-*T_c* superconductivity.

Introduction

Iridates with strong spin-orbit coupling effects can generate exotic quantum phenomena, such as quantum spin liquid phases, Kitaev magnetism, and possible superconductivity.¹⁻⁴ Different from most $3d$ transition metal oxides in which the spin and orbit can be distinct in the energy scale, the spin and orbit interact heavily in $5d$ transition metal oxides. Among the Mott insulating $5d$ transition metal oxides, Sr_2IrO_4 ⁵⁻⁹ has attracted significant attention due to its similarity to cuprate high-temperature superconductor, La_2CuO_4 ¹⁰⁻¹². As a single-layer Ruddlesden–Popper compound, Sr_2IrO_4 crystallizes in a tetragonal lattice with an inversion center ($I4_1/acd$, #142) at ambient pressure. Sr_2IrO_4 contains stacked IrO_2 square lattices where the unit cell is doubled compared to the CuO_2 square lattices in high- T_c cuprates as a result of a staggered rotation of IrO_6 octahedron. Although superconductivity is not yet confirmed, many phenomena characteristic of the superconducting cuprates have been observed in electron- and hole-doped iridates including pseudogaps, Fermi arcs, and d -wave gaps.¹³⁻¹⁵ The $\text{Ir-}d^5$ electrons in regular IrO_6 octahedron occupy the t_{2g} orbitals, which can be approximated as two fully filled spin-orbital coupled $J_{\text{eff}} = 3/2$ bands and one half-filled $J_{\text{eff}} = 1/2$ band. The J_{eff} band is split into an upper and lower Hubbard band by on-site Coulomb interaction. According to a previous study, as Sr_2IrO_4 is cooled below its Néel temperature (T_N , ~ 230 K), the spin-orbit coupled $J_{\text{eff}} = 1/2$ moments order into a basal plane commensurate Néel state. Octahedral rotations in Sr_2IrO_4 allow for non-zero Dzyaloshinskii-Moriya (DM) interactions that results in a canting of the ordered moments away from the crystallographic axis and a weak ferromagnetic moment per layer.¹⁶ Such a magnetic transition maintains the inversion symmetry but lowers the rotational symmetry of the system from C_4 to C_2 . However, no additional symmetry breaking has been observed by neutron or X-ray diffraction, which makes the comparison of the iridate to cuprate phenomenology incomplete. To date, multiple methods have been used to tune the Mott insulating states in Sr_2IrO_4 , for example, isovalent Rh doping on the Ir site.^{5,17-23} After partially substituting Ir with Rh, an insulator-to-metal transition can be detected. However, high pressure was also used to tune the electronic states up to 55 GPa without observing any metallic state in Sr_2IrO_4 .^{24,25}

In this report, we applied the high-pressure (6 GPa) high-temperature (1400 °C) method for synthesizing Sr_2IrO_4 . Under such extreme conditions, the obtained Sr_2IrO_4 remains in a tetragonal structure but without an inversion center. The space group was determined by single-

crystal X-ray diffraction (SC-XRD) as $I4mm$ (#107). Unlike the ambient pressure phase, the high-pressure phase consists of the single layered IrO_2 square lattice, just like CuO_2 square in cuprate. Magnetic susceptibility measurement on high pressure Sr_2IrO_4 indicate a magnetic ordering temperature of approximately 86 K, which is dramatically lower than ambient pressure Sr_2IrO_4 . Interestingly, the resistivity data shows three-dimensional Mott variable-range hopping of charge carriers between states localized by disorder with negligible long-range Coulomb interactions. Discovering the non-centrosymmetric phase in Sr_2IrO_4 may accelerate the realization of superconductivity and unravel the puzzle in cuprate high- T_c superconductors.

Experimental Section

High-Pressure Synthesis. The ambient pressure Sr_2IrO_4 phase was prepared accordingly by thoroughly mixing and pelletizing the materials SrCO_3 and IrO_2 and subsequently heating them to 900 °C then regrinding and reannealing at 1000 °C and subsequently reannealing at 1100 °C.²⁶ The ambient pressure Sr_2IrO_4 was pressurized to 6 GPa in 24 hours. After that, the sample was heated up to 1400 °C and stayed at 1400 °C for 4 hours. Another sample was heated to 1400 °C and stayed up to 28 hours to explore the optimal condition. The sample was cooled down to room temperature before depressurizing to the ambient pressure. The high-pressure synthesis was performed by statically compressing the sample using the Walker type multi-anvil press²⁷ where the original Sr_2IrO_4 was placed in a Pt capsule inside an Al_2O_3 crucible that was inserted into a Cermacast 646 octahedra pressure medium lined on the inside with a LaCrO_3 heater.

Phase Analysis and Chemical Composition Determinations. The phase identity and purity were examined using a Bruker D2 Phaser powder X-ray diffractometer with Cu $K\alpha$ radiation ($\lambda = 1.5406 \text{ \AA}$). Room temperature measurements were performed with a step size of 0.004° at a scan speed of $0.55^\circ/\text{min}$ over a Bragg angle (2θ) range of $5\text{--}90^\circ$. FullProf Suite software^{28,29} was utilized to analyze the phase information and lattice parameters from a Rietveld refinement.

Structure Determination. The room temperature and low temperature (100 K) crystal structure was determined using a Bruker D8 Quest Eco single crystal X-ray diffractometer, equipped with Mo radiation ($\lambda_{K\alpha} = 0.71073 \text{ \AA}$) with an ω of 2.0° per scan and an exposure time of 10 s per frame. A SHELXTL package with the direct methods and full-matrix least-squares on the F^2 model was used to determine the crystal structure of Sr_2IrO_4 .^{30,31} To confirm the crystal structure, high-resolution scanning transmission electron microscopy (HR-STEM) images were collected and electron diffraction was conducted using a 200 kV JEOL ARM electron microscope equipped with double aberration correctors. Samples for TEM analysis were crushed in an agate mortar and deposited directly onto a holey carbon copper grid.

Physical Properties Measurement. Temperature and field-dependent magnetization, resistivity, and heat capacity measurements were performed with a Quantum Design physical property measurement system (PPMS) under a temperature range of 1.85–300 K and applied fields up to 9

T. Electrical resistivity measurements were accomplished with a four-probe method using platinum wires on a pelletized sample of Sr_2IrO_4 . The polycrystalline Sr_2IrO_4 was pressed up to 6 GPa and heated at a lower temperature (100 °C) to eliminate the contribution of grain boundary effect but also keep the phase stable.

Results and Discussions

Exploring New Phase. The new Sr_2IrO_4 phase ($I4mm$, #107) was formed at 6 GPa from the starting material, ambient pressure Sr_2IrO_4 ($I4_1/acd$, #142). The synthesis temperatures were set up at 1200 °C and 1400 °C. The high pressure Sr_2IrO_4 phase was only produced at 1400 °C. To increase the yield and grow larger crystals, the longer heating duration of 28 hours was tested. However, the secondary tetragonal phase $\text{Sr}_3\text{Ir}_2\text{O}_7$ simultaneously forms once the heating duration was increased. As a result, only 4 hours heating process can produce the specimen consisting mostly of pure phase. The resulting Le Bail fitting of the PXRD patterns for the high-pressure phase Sr_2IrO_4 is shown in **Fig. 1**. An overlay of the PXRD patterns in **Fig. S1** demonstrates the formation of the secondary $\text{Sr}_3\text{Ir}_2\text{O}_7$ phase. The pure phase synthesized at 1400 °C for 4 hours was used for the physical property measurements below.

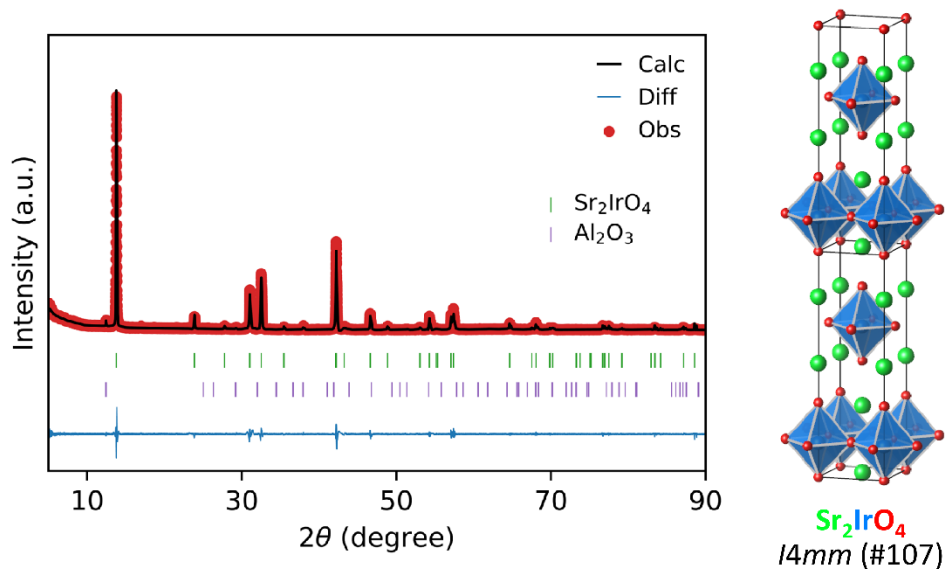


Fig. 1 Powder X-ray diffraction pattern of the high-pressure Sr_2IrO_4 phase. The experimental data (red dots) was modeled with a Rietveld refinement (black line). The blue line indicates the corresponding residual pattern (difference between observed and calculated patterns) along with Bragg peak positions for Sr_2IrO_4 (green) and Al_2O_3 (purple) represented by the vertical tick marks.

Crystal Structure and Phase Determination. After 4 hours of treatment at 6 GPa and 1400 °C, single crystals of Sr₂IrO₄ were formed, subsequently selected, and measured at both 300 K and 100 K using the single crystal X-ray diffractometer. High-pressure Sr₂IrO₄ crystallizes with good agreement into the tetragonal space group *I4mm*, as indicated by the single crystal X-ray diffraction (SCXRD) refinement information listed in Table S1. Similar to ambient pressure Sr₂IrO₄, the high pressure Sr₂IrO₄ phase contains the layers of IrO₆ octahedra with intercalated Sr atoms. The differences between these two are half-*c* lattice, the disappearance of the inversion center because of the nonsymmetric distortion of IrO₆ octahedra, and the disappearance of IrO₆ octahedral rotations in the *ab*-plane in high-pressure Sr₂IrO₄ compared to the ambient pressure phase. Shown in **Fig. 2** are crystal structures and IrO₆ octahedra stacking view of ambient pressure Sr₂IrO₄ (*I4₁/acd*), high-pressure Sr₂IrO₄ (*I4mm*), and previously reported La₂CuO₄ (*I4/mmm*), with Ir-O atomic distance in the IrO₆ octahedra highlighted. Atomic site vacancies and site disorder were considered and refined to reveal the O3 atomic site is slightly displaced from the closer ideal *4b* site ($1/2, 0, z$) to the *8d* site ($x, 0, z$) having a statistical occupancy of 0.5. The disordered model yielded a more reasonable refinement with an *R* factor of 4.35 and goodness of fit (GOF) of 1.177 while having only one O3 atomic site resulted in an *R* factor of 4.62 and GOF of 1.305. As such an angle δ can be determined from $(1/2 \pm \delta, 0, z)$ with respect to an IrO₆ octahedra where the O3 atoms occupy the *4b* site. This structural disorder has been thoroughly discussed for the ambient pressure Sr₂IrO₄ structure.³² Additionally, the high-pressure Sr₂IrO₄ phase possesses a nonsymmetric IrO₆ octahedra elongation along the *c* axis, ranging in Ir-O atomic distance from 1.94(6)–2.27(6) Å, as indicated in **Fig. 2b**, which is in fact the cause of noncentrosymmetric structural character. This behavior is kind of similar to the prominent feature of ambient pressure Sr₂IrO₄ that has been speculated to originate from a Jahn Teller distortion.³³⁻³⁵ Previous studies under high-pressure have revealed an increase in the IrO₆ octahedra elongation with pressurization.^{36,37} Compared to ambient pressure Sr₂IrO₄, one Ir-O along the *c* -axis is significantly elongated, with the other almost remains the same, i.e., one oxygen atom is driven away from the Ir atom, and thus the repulsion between Ir and the oxygen ligand is reduced. This will lower the energy of orbitals that contains *z* contribution and split *e_g* and *t_{2g}* orbitals, making the crystal field split of Ir *d* orbitals even more complicated. Together with spin-orbit coupling, this may further remove orbital degeneracies. Moreover, as pressure applied for Sr₂IrO₄, the Ir-O-

Ir angle was pushed close to 180° , which is the angle in Cu-O-Cu in La_2CuO_4 . The structural disorder was further confirmed at 100 K and the SCXRD refinement details can be found in SI.

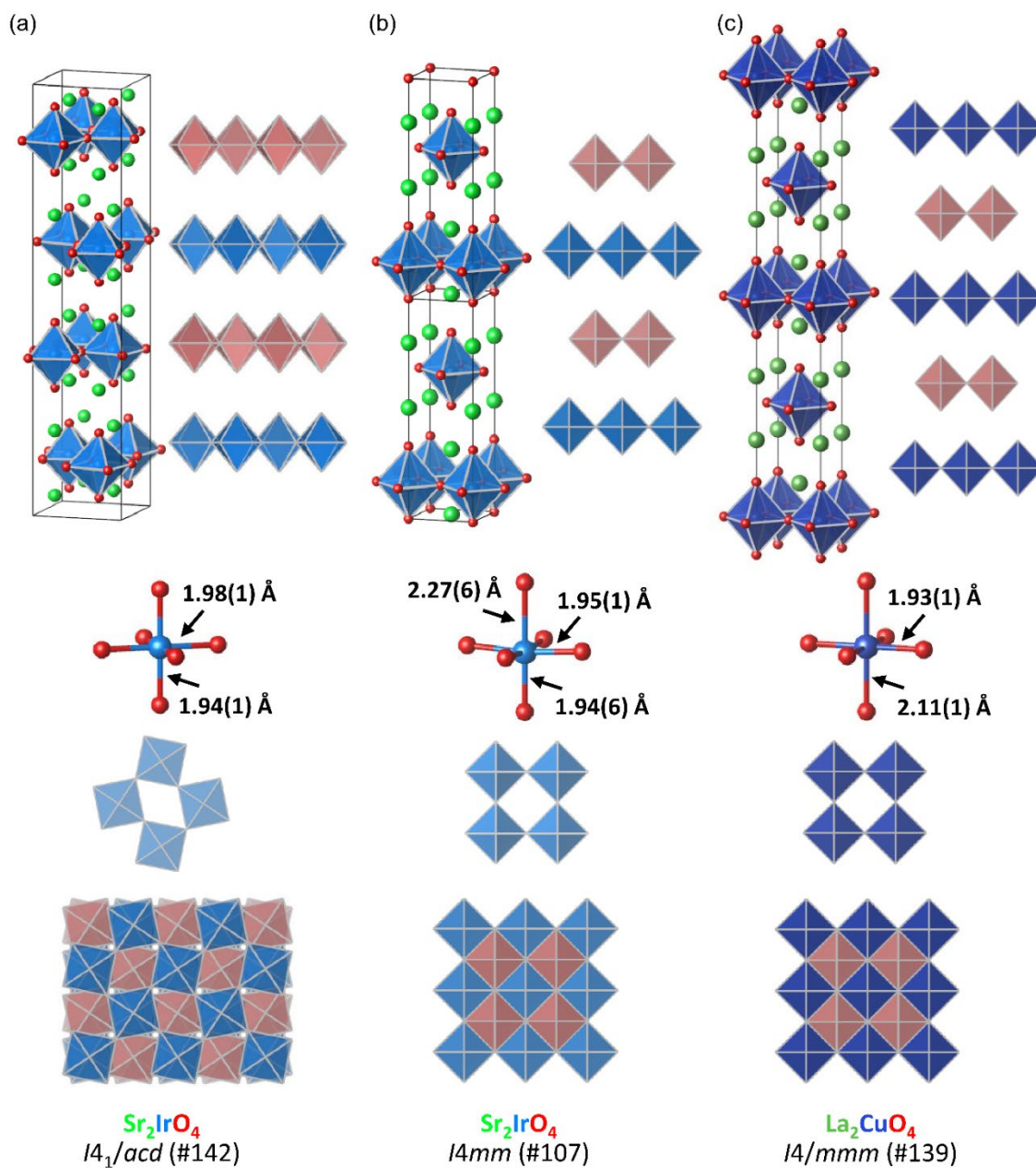


Fig. 2 Crystal structure illustration. Crystal structures, octahedra stacking view along a axis, and along c axis of (a) ambient pressure Sr_2IrO_4 , (b) as-synthesized high pressure Sr_2IrO_4 , and (c) previously reported La_2CuO_4 , with Ir(Cu)O₆ octahedra and Ir(Cu)-O atomic distances presented. Green, blue, dark green, dark blue, and red atoms represent Sr, Ir, La, Cu, and O atoms, respectively. Single-layer square net is also highlighted.

Transmission Electron Microscopy. The non-centrosymmetric space group and loss of IrO_6 octahedral rotation, as well as the oxygen distortion and defects in Sr_2IrO_4 , can at first, be surprisingly interesting, thus high-pressure Sr_2IrO_4 was investigated by transmission electron microscopy (TEM) to characterize its crystallographic nature. The High-angle annular dark-field scanning transmission electron microscopy (HAADF-STEM) image was obtained along the a axis shown in **Fig. 3a**. The TEM diffraction patterns projected down the crystalline $[100]$ axis (**Fig. 3b**) allowed for the determination of the orientation of the images through the d_{002} spacing. The c -axis parameter is $\sim 12.8 \text{ \AA}$, agreeing with the single crystal XRD results. The electron diffraction and imaging study confirmed the high quality of the nanoscale ordering in the specimen. However, the fractional spots $1/2$ $(110)/(1-10)$ were observed by TEM electron diffraction in **Fig. 3d**. As is known that IrO_6 tilt/rotation along the c -axis would not introduce these fractional spots. Such fractional reflection spots are related to the ordering of oxygen vacancy, which is consistent with single crystal X-ray diffraction results in **Fig. 3e**.

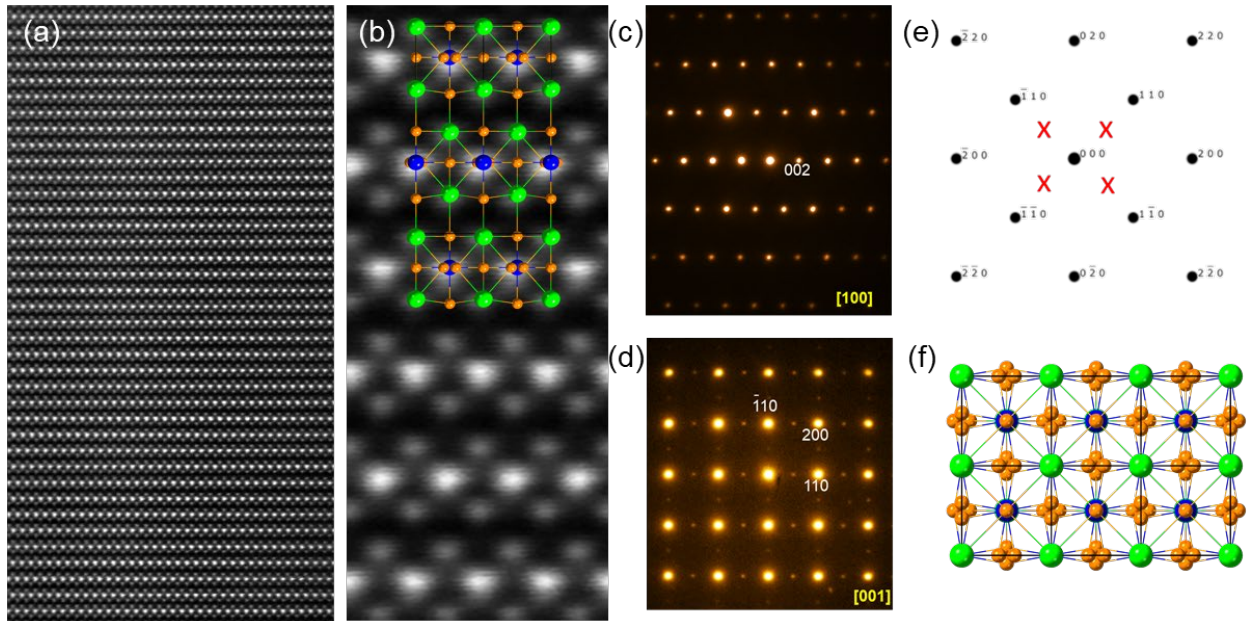


Fig. 3 Transmission electron microscopy study of high pressure Sr_2IrO_4 phase. (a) HAADF-STEM image taken along a axis from a large area showing the high quality of the crystal Sr_2IrO_4 . (b) The zoom-in HAADF image shows the projected structure in the $[100]$ direction, with a crystal model superimposed, where Sr (green), Ir (blue), and O (orange). (c) The diffraction pattern took along the $[100]$ direction which is consistent with the simulated pattern (**Fig. 3e**) based on the crystal model determined by single crystal X-ray diffraction. (d) SAED pattern along the $[001]$ direction showing fractional spots of $1/2$ $(110)/(1-10)$. (e) Simulated diffraction pattern and (f) projected crystal structure along the $[001]$ direction based on the crystal structure determined by

SCXRD. The fractional spots observed in TEM were marked in red. The single crystal structure of Sr₂IrO₄ with oxygen distortion was confirmed by both single crystal X-ray diffraction and TEM.

Weak Ferromagnetic Ordering. To study the magnetic properties of the high pressure Sr₂IrO₄ phase, the temperature-dependent susceptibility was measured under field cooled warming (FCW) and field cooled cooling (FCC) mode at 0.1 T shown in **Fig. 4a**. No significant differences between FCW and FCC were observed. At about 150 K, the susceptibility goes below 0, indicating a diamagnetic contribution in the system, which suggests the possible breakdown of Curie-Weiss behavior at high temperatures in the system. The data between 80–140 K was modeled with the modified Curie-Weiss law (**Eqn. 1**), shown in **Fig. 4b** and **Fig. S2b**,

$$\chi = \chi_0 + \frac{C}{T - \theta_{cw}} \quad (1)$$

where θ_{cw} is the paramagnetic Curie temperature, χ_0 is the temperature independent susceptibility and C is the Curie constant. From the fitting, the Curie temperature, θ_{cw} , of 86(7) K was found to be comparable to the magnetic ordering temperature $T_c \sim 84$ K, as determined from the minimum in the temperature derivative of χ (See **Fig. S2a** for details). The magnetic ordering temperature, consequently, decreases when compared to ambient pressure Sr₂IrO₄, which has a $T_c \sim 240$ K.^{39,40} On the other hand, it can be assumed that the T_c significantly decreases as the angle of Ir-O-Ir is more close to 180 °, which is the one observed in Cu-O-Cu in high T_c superconductor La₂CuO₄. The fitting also gave a negative χ_0 of $-2.9(9) \times 10^{-3}$ emu mol⁻¹ Oe⁻¹, which provided a potential opportunity to extrapolate our Curie-Weiss fit to higher temperature. Finally, up to 160 K was included (**Fig. S2c**) and the fit yielded the effective moment $\mu_{\text{eff}} = 1.2(2)$ μ_B/Ir , which is more agreeable with the Hund's-rule value of 1.73 μ_B/Ir for $S = 1/2$ than the reported $\mu_{\text{eff}} = 0.33$ μ_B/Ir for ambient pressure Sr₂IrO₄.

Furthermore, the magnetization of high pressure Sr₂IrO₄ was measured as shown in **Fig. 4c** up to 9 T at different temperatures. It appears to saturate at ~ 3 T at which the magnetic saturation moment (μ_{sat}) was determined to be ~ 0.046 μ_B/Ir . This value is significantly lower than the theoretical value of $1/3$ μ_B f.u⁻¹, however, similar to the previously reported moment for the ambient pressure Sr₂IrO₄ phase, which originates from spin canted antiferromagnetic (AFM) order.³⁹ This could also explain why the weak ferromagnetic behavior observed in the temperature

dependence of magnetic susceptibility gives such a low value of moment. However, unlike the ambient pressure Sr_2IrO_4 phase, the magnetization reaches a maximum at around 3 T at which point the magnetization decreases. It turned out that diamagnetic transition was observed under higher fields at the respective temperatures (e.g., see the 50 K and 100 K data). At 300 K, a complete diamagnetic behavior was shown, consistent with $\chi < 0$ shown in **Fig. 4c**. Subtracting this by linearly fitting data from 7–9 T, the μ_{sat} was modified to be $0.067 \mu_B/\text{Ir}$ at 2 K and $0.014 \mu_B/\text{Ir}$ at 100 K, as presented in **Fig. 4d** and **4e**. Magnetic hysteresis was observed in the system under 2 K from -0.6 T to 0.6 T, presented in **Fig. S3**, which could be interpreted as small canting of the moments existed in the system.

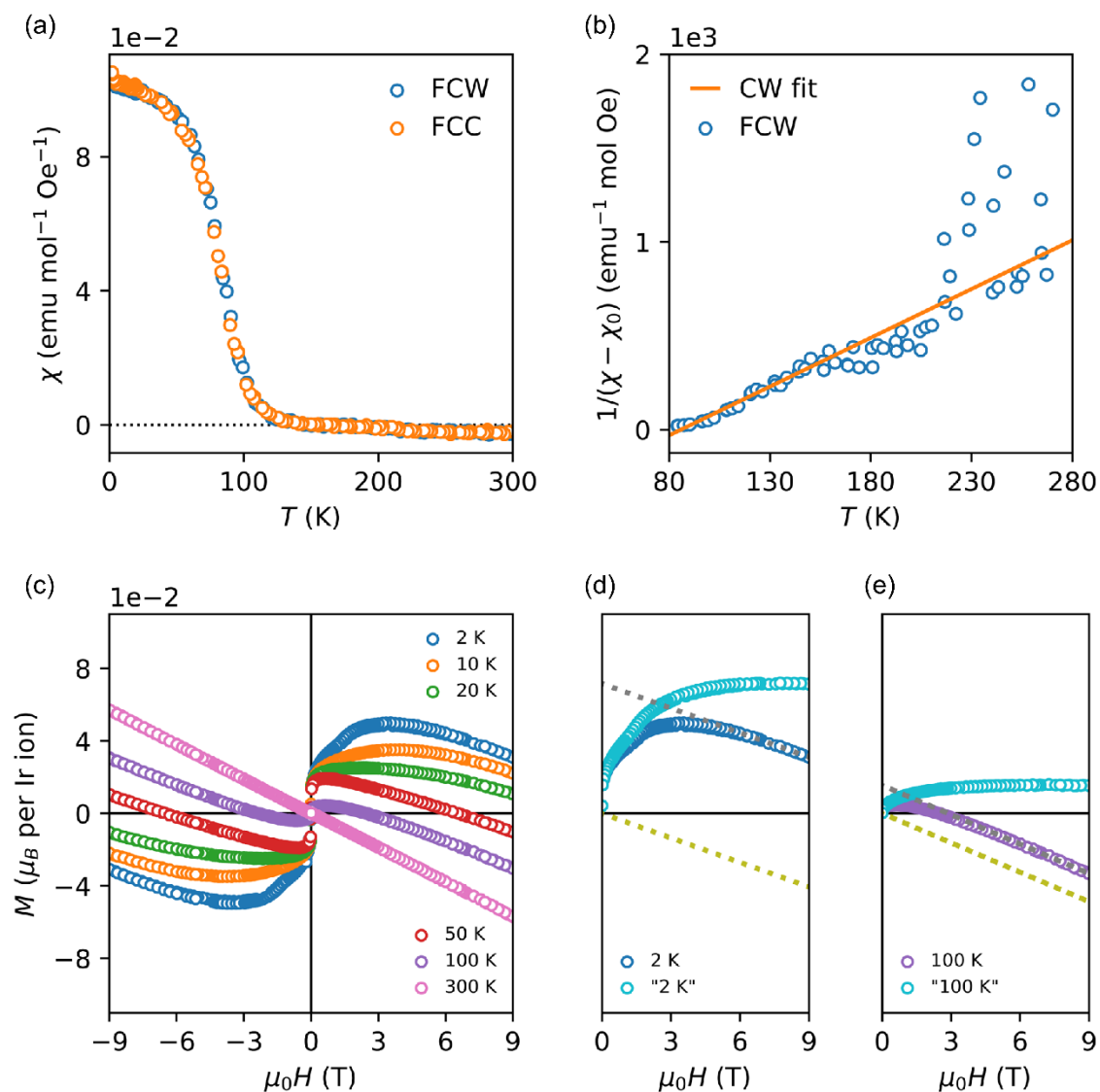


Fig. 4 Magnetization in the dependence of temperature and field. (a) Temperature dependence of magnetic susceptibility χ at 1000 Oe under FCW and FCC mode ranging from 2–300 K. No significant difference was observed. (b) The modified inverse magnetic susceptibility data (FCW, 80–140 K, blue hollow circle) fitted with the modified Curie-Weiss model (orange line). (c) Field dependence of magnetization up to 9 T at different temperatures. (d) Derivation of μ_{sat} at 2 K by linearly fitting the magnetization data from 7–9 T. (e) Derivation of μ_{sat} at 100 K.

No Magnetically Induced Anomalies Observed in Specific Heat Measurement. To confirm the magnetic transition, the specific heat over the temperature range of 2–200 K was measured under 0 T with a polycrystalline pelletized sample of Sr₂IrO₄, as presented in **Fig. 5a**. Measurements

under applied fields of 0.05 T and 1 T in **Fig. S3** were additionally tested to conclude no significant deviation from the 0 T specific heat. No λ shape anomalies were observed at the whole temperature regime studied, which may result from higher temperature regions being heavily dominated by the phonon contribution. The specific heat data were fitted by the Debye model (**Eqn. 2**), and Einstein model (**Eqn. 3**), shown in **Fig. S4a** and **b**. The Debye and Einstein temperatures could then be determined as 417(2) K and 306(2) K, respectively. However, neither of these two described the experimental data well.

$$C_D = 9nR \left(\frac{T}{\theta_D} \right)^3 \int_0^{\theta_D/T} \frac{x^4 e^x}{(e^x - 1)^2} dx \quad (2)$$

where n is the number of atoms per formula unit, R is the gas constant, and θ_D is the Debye temperature.

$$C_E = 3nR \left(\frac{\theta_E}{T} \right)^2 e^{\frac{\theta_E}{T}} \left(e^{\frac{\theta_E}{T}} - 1 \right)^{-2} \quad (3)$$

where n is the number of atoms per formula unit, R is the gas constant, and θ_E is the Einstein temperature.

The specific heat data was further fitted with two Debye model (**Eqn. 4**) and weighted Debye model (**Eqn. 5**), with and without the electronic contribution included, shown in **Fig. 5a** and **Fig. S4c, d, and e**. The data was found to be described well with two Debye model (**Fig. 5a**), and the Debye temperatures, θ_{D1} of 235(1) K, θ_{D2} of 708(5) K was obtained. At low temperatures, the first Debye mode has a larger contribution to the specific heat. Within the temperature regime studied, the expected Dulong-Petit value of $3nR$ is not recovered, and this can be explained by the high value of θ_{D2} , which means that the specific heat will plateau at $T \gg \theta_{D2}$. The fitting also yields s_{D1} of 3.20(3) and s_{D2} of 4.51(2). The sum of these two seems a little larger than the expected value of 7 for Sr_2IrO_4 , which may be attributed to the impurity of $\text{Sr}_{n+1}\text{Ir}_n\text{O}_{3n+1}$, lack of electron contribution, or overestimation of photon contribution in the model. Once the electron contribution term was included, θ_{D1} was slightly shifted to 238(2) K and the sum of s_{D1} and s_{D2} went down to 7.52(11).

$$C = 9s_{D1}R \left(\frac{T}{\theta_{D1}} \right)^3 \int_0^{\theta_{D1}/T} \frac{x^4 e^x}{(e^x - 1)^2} dx + 9s_{D2}R \left(\frac{T}{\theta_{D2}} \right)^3 \int_0^{\theta_{D2}/T} \frac{x^4 e^x}{(e^x - 1)^2} dx (+\gamma T) \quad (4)$$

where θ_{D1} and θ_{D2} are Debye temperatures, s_{D1} and s_{D2} are the oscillator strengths, and γT is the electron contribution.

$$C = 9s_D R \left(\frac{T}{\theta_D}\right)^3 \int_0^{\theta_D/T} \frac{x^4 e^x}{(e^x - 1)^2} dx + 3s_E R \left(\frac{\theta_E}{T}\right)^2 e^{\frac{\theta_E}{T}} \left(e^{\frac{\theta_E}{T}} - 1\right)^{-2} (+\gamma T) \quad (5)$$

where θ_D and θ_E are the Debye and Einstein temperatures, s_D and s_E are the oscillator strengths.

It should be noted that the magnetic contribution cannot be quantitatively extracted from the specific heat data as the phonon contribution cannot be distinguished from the magnetic contribution due to the lack of a nonmagnetic analog.

At a low-temperature regime, of 2–20 K, the specific heat was measured, as shown in **Fig. S5**. The data ranging from 2–3.2 K was fitted with **Eqn. 6**, shown in **Fig. 5b**.

$$\frac{C_p}{T} = \gamma + \beta T^2 \quad (6)$$

From this fitting, a γ and β value of 0.0153(2) J mol⁻¹ K⁻² and 7.1(2) × 10⁻⁴ J mol⁻¹ K⁻³ corresponding to the electronic and phonon contributions to the specific heat, respectively, could be obtained. The β value recovered the Debye temperature (**Eqn. 7**) to be 268(2) K, which is much closer to θ_{D1} rather than θ_{D2} . It falls out of the temperature interval, 300–350 K, where iridates most commonly exhibit Debye temperatures.⁴¹

$$\theta_D = \left(\frac{12\pi^4}{5\beta} nR\right)^{\frac{1}{3}} \quad (7)$$

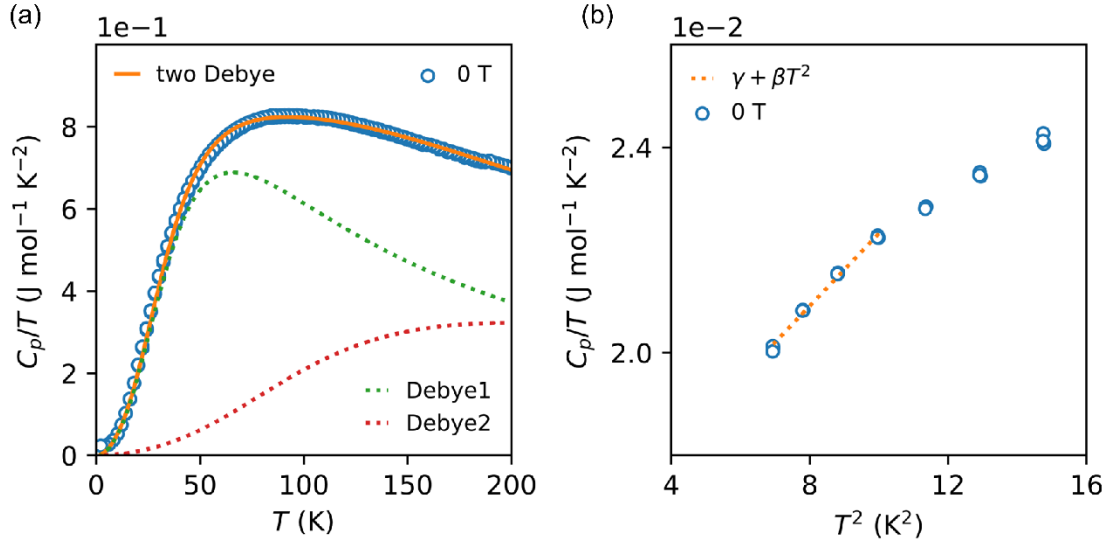


Fig. 5 Specific heat data fitting of high pressure Sr_2IrO_4 . (a) Temperature dependence of specific heat over temperature (C_p/T) for high-pressure Sr_2IrO_4 fitted by two Debye model in orange. Green and red dotted lines refer to the 1st and 2nd Debye model. (b) C_p/T vs T^2 between 2–3.2 K fitted with Eqn. 6 (orange dotted line).

Mott Variable-range Hopping (VRH). It is critical to investigate the electrical conductivity in the high pressure Sr_2IrO_4 phase to compare to the Mott insulator ambient pressure Sr_2IrO_4 . Temperature-dependent resistivity measurements were performed from 2–300 K with an applied field up to 9 T on a pelletized polycrystalline sample of the high pressure Sr_2IrO_4 phase, shown in Fig. 6a. No significant field dependence was observed, which indicates the insignificance of magnetoresistance for the high pressure Sr_2IrO_4 phase. This may be not unexpected considering the small saturation moment under fields (see the discussion above). At room temperature and 0 T, the resistivity is relatively low, only around 4 Ω cm. However, the resistivity is increases by 6 orders of magnitude upon cooling, indicating the semiconducting character of the high-pressure Sr_2IrO_4 phase.

To further analyze its behavior, we first tried to model the temperature dependence of ρ with the Arrhenius law (Eqn. 8),

$$\rho = \rho_0 e^{E_p/kT} \quad (8)$$

where ρ_0 is the residual resistivity, E_ρ is the activation energy, and k is the Boltzmann constant. However, ρ could not be fitted well to a E_ρ , shown in **Fig. S7a**, i.e., the Arrhenius law is not well obeyed. Then its temperature dependence was fitted by law in the form (**Eqn. 9**) with ν of 1/2 and 1/4,

$$\rho = \rho_0 e^{(T_0/T)^\nu} \quad (9)$$

where ρ_0 is the residual resistivity, and T_0 is the characteristic temperature. The fitting results were presented in **Fig. 6b**, and **Fig. S8**, with parameters summarized in **Table S4**. The value ν of 1/4 is favored over 1/2. While both of them indicate three-dimensional Mott variable-range hopping of charge carriers between localized states, the weaker temperature dependence with ν of 1/4 implies negligible long-range Coulomb interactions between localized electrons in the temperature regime studied. This behavior is also reported in the ambient pressure Sr_2IrO_4 .⁴² To explore the harboring quantum states in the high-pressure Sr_2IrO_4 phase, further examination of its transport properties is warranted.

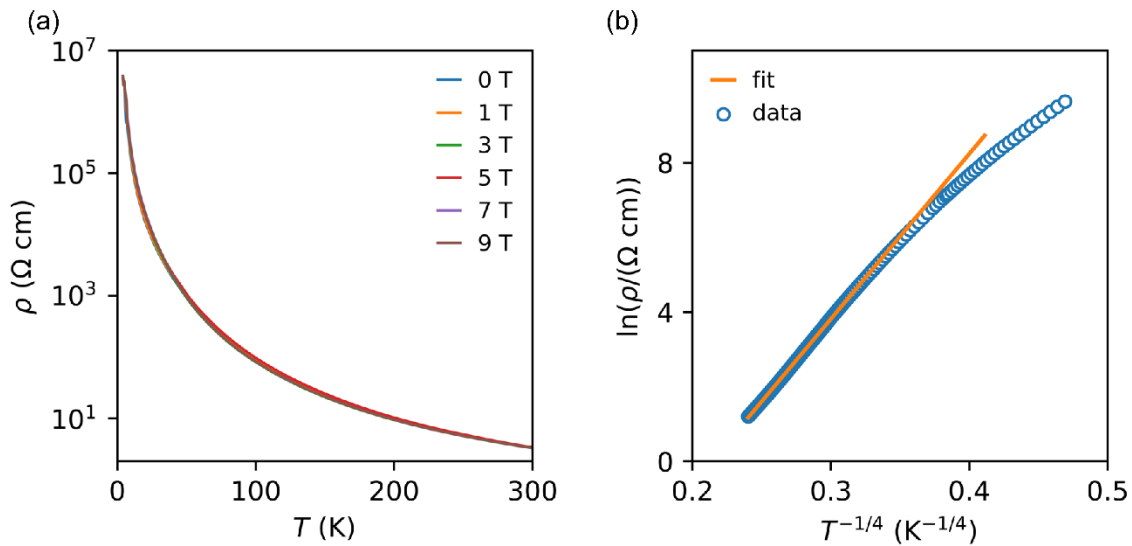


Fig. 6 Details of field and temperature dependent resistivity. (a) Temperature dependence of resistivity data for high-pressure phase Sr_2IrO_4 under fields up to 9 T. No significant derivation was observed. **(b)** The resistivity ρ (blue hollow circle) ranging from 80–300 K was fitted by **Eqn. 9** with ν of 1/4 (orange line). A linear relationship was obtained.

Conclusion

In summary, we reported the non-centrosymmetric Sr₂IrO₄ phase obtained under high pressure and high temperature conditions. The ferromagnetic ordering temperature decreases significantly to $T_c \sim 86$ K from ~ 240 K in the ambient pressure Sr₂IrO₄, while there may be a possible breakdown of the Curie-Weiss law under higher temperatures. Diamagnetism was observed under room temperature and higher fields. No anomalies indicating magnetic ordering were observed in the specific heat measurements, where a greater phonon contribution was obtained from the low-temperature regime. Temperature-dependent resistivity revealed three-dimensional Mott variable-range hopping of charge carriers between states localized by disorder with negligible long-range Coulomb repulsions. Further transport measurements, together with first-principles calculation, are expected to explore the electronic properties of the high-pressure Sr₂IrO₄ phase. Such a system may offer a promising platform to unravel the mystery of high- T_c superconductivity in cuprates.

Acknowledgments

The work at Rutgers was supported by U.S. DOE-BES under Contract DE-SC0022156. The electron microscopy work at BNL was supported by U.S. DOE-BES, Materials Sciences and Engineering Division under Contract No. DESC0012704.

Supporting Information

Single crystal X-ray diffraction data at room temperature and 100 K; Anisotropic displacement parameters; Atomic coordinates and equivalent isotropic displacement parameters; PXRD overlay of Sr₂IrO₄; Magnetic susceptibility and Curie-Weiss fitting; Magnetic hysteresis; Field dependence of specific heat; Specific heat data fitted by Debye and Einstein model; Low temperature specific heat data (2–20 K); Temperature dependence of resistivity; Resistivity data fitted by Eqn. 9 with ν of 1/2 and 1/4; Summary of fitting parameters for resistivity data.

References

1. Takagi, H.; Takayama, T.; Jackeli, G.; Khaliullin, G.; Nagler, S. E. Concept and realization of Kitaev quantum spin liquids. *Nat. Rev. Phys.* **2019**, *1*, 264-280.
2. Revelli, A.; Moretti Sala, M.; Monaco, G.; Hickey, C.; Becker, P.; Freund, F.; Jesche, A.; Gegenwart, P.; Eschmann, T.; Buessen, F. L.; Trebst, S.; van Loosdrecht, P. H. M.; van den Brink, J.; Grüninger, M. Fingerprints of Kitaev physics in the magnetic excitations of honeycomb iridates. *Phys. Rev. Res.* **2020**, *2*, 043094.
3. Gao, Y.; Zhou, T.; Huang, H.; Wang, Q.-H. Possible superconductivity in Sr₂IrO₄ probed by quasiparticle interference. *Sci. Rep.* **2015**, *5*, 9251.
4. Mitchell, J. F. Sr₂IrO₄: Gateway to cuprate superconductivity? *APL Mater.* **2015**, *3*, 062404.
5. Cao, Y.; Wang, Q.; Waugh, J. A.; Reber, T. J.; Li, H.; Zhou, X.; Parham, S.; Park, S. R.; Plumb, N. C.; Rotenberg, E.; Bostwick, A.; Denlinger, J. D.; Qi, T.; Hermele, M. A.; Cao, G.; Dessau, D. S. Hallmarks of the Mott-metal crossover in the hole-doped pseudospin-1/2 Mott insulator Sr₂IrO₄. *Nat. Commun.* **2016**, *7*, 11367.
6. Nichols, J.; Bray-Ali, N.; Ansary, A.; Cao, G.; Ng, K.-W. Tunneling into the Mott insulator Sr₂IrO₄. *Phys. Rev. B* **2014**, *89*, 085125.
7. Kim, B. J.; Jin, H.; Moon, S. J.; Kim, J. Y.; Park, B. G.; Leem, C. S.; Yu, J.; Noh, T. W.; Kim, C.; Oh, S. J.; Park, J. H.; Durairaj, V.; Cao, G.; Rotenberg, E. Novel $J_{\text{eff}}=1/2$ Mott State Induced by Relativistic Spin-Orbit Coupling in Sr₂IrO₄. *Phys. Rev. Lett.* **2008**, *101*, 076402.
8. Kim, B. J.; Ohsumi, H.; Komesu, T.; Sakai, S.; Morita, T.; Takagi, H.; Arima, T. Phase-Sensitive Observation of a Spin-Orbital Mott State in Sr₂IrO₄. *Science* **2009**, *323*, 1329-1332.
9. Ye, F.; Chi, S.; Cao, H.; Chakoumakos, B. C.; Fernandez-Baca, J. A.; Custelcean, R.; Qi, T. F.; Korneta, O. B.; Cao, G. Direct evidence of a zigzag spin-chain structure in the honeycomb lattice: A neutron and x-ray diffraction investigation of single-crystal Na₂IrO₃. *Phys. Rev. B* **2012**, *85*, 180403.
10. Grant, P. M.; Parkin, S. S. P.; Lee, V. Y.; Engler, E. M.; Ramirez, M. L.; Vazquez, J. E.; Lim, G.; Jacowitz, R. D.; Greene, R. L. Evidence for superconductivity in La₂CuO₄. *Phys. Rev. Lett.* **1987**, *58*, 2482-2485.
11. Dean, M. P. M.; Springell, R. S.; Monney, C.; Zhou, K. J.; Pereiro, J.; Božović, I.; Dalla Piazza, B.; Rønnow, H. M.; Morenzoni, E.; van den Brink, J.; Schmitt, T.; Hill, J. P. Spin excitations in a single La₂CuO₄ layer. *Nat. Mater.* **2012**, *11*, 850-854.
12. Attfield, J. P.; Kharlanov, A. L.; McAllister, J. A. Cation effects in doped La₂CuO₄ superconductors. *Nature* **1998**, *394*, 157-159.
13. Battisti, I.; Bastiaans, K. M.; Fedoseev, V.; de la Torre, A.; Iliopoulos, N.; Tamai, A.; Hunter, E. C.; Perry, R. S.; Zaanen, J.; Baumberger, F.; Allan, M. P. Universality of pseudogap and emergent order in lightly doped Mott insulators. *Nat. Phys.* **2017**, *13*, 21-25.
14. Kim, Y. K.; Sung, N. H.; Denlinger, J. D.; Kim, B. J. Observation of a d-wave gap in electron-doped Sr₂IrO₄. *Nat. Phys.* **2016**, *12*, 37-41.

15. He, J.; Hafiz, H.; Mion, T. R.; Hogan, T.; Dhital, C.; Chen, X.; Lin, Q.; Hashimoto, M.; Lu, D. H.; Zhang, Y.; Markiewicz, R. S.; Bansil, A.; Wilson, S. D.; He, R.-H. Fermi Arcs vs. Fermi Pockets in Electron-doped Perovskite Iridates. *Sci. Rep.* **2015**, *5*, 8533.
16. Zhao, L.; Torchinsky, D. H.; Chu, H.; Ivanov, V.; Lifshitz, R.; Flint, R.; Qi, T.; Cao, G.; Hsieh, D. Evidence of an odd-parity hidden order in a spin-orbit coupled correlated iridate. *Nat. Phys.* **2016**, *12*, 32-36.
17. Chikara, S.; Fabbris, G.; Terzic, J.; Cao, G.; Khomskii, D.; Haskel, D. Charge partitioning and anomalous hole doping in Rh-doped Sr₂IrO₄. *Phys. Rev. B* **2017**, *95*, 060407.
18. Sohn, C. H.; Cho, D.-Y.; Kuo, C. T.; Sandilands, L. J.; Qi, T. F.; Cao, G.; Noh, T. W. X-ray Absorption Spectroscopy Study of the Effect of Rh doping in Sr₂IrO₄. *Sci. Rep.* **2016**, *6*, 23856.
19. Qi, T. F.; Korneta, O. B.; Li, L.; Butrouna, K.; Cao, V. S.; Wan, X.; Schlottmann, P.; Kaul, R. K.; Cao, G. Spin-orbit tuned metal-insulator transitions in single-crystal Sr₂Ir_{1-x}Rh_xO₄. *Phys. Rev. B* **2012**, *86*, 125105.
20. Clancy, J. P.; Lupascu, A.; Gretarsson, H.; Islam, Z.; Hu, Y. F.; Casa, D.; Nelson, C. S.; LaMarra, S. C.; Cao, G.; Kim, Y.-J. Dilute magnetism and spin-orbital percolation effects in Sr₂Ir_{1-x}Rh_xO₄. *Phys. Rev. B* **2014**, *89*, 054409.
21. Ye, F.; Wang, X.; Hoffmann, C.; Wang, J.; Chi, S.; Matsuda, M.; Chakoumakos, B. C.; Fernandez-Baca, J. A.; Cao, G. Structure symmetry determination and magnetic evolution in Sr₂Ir_{1-x}Rh_xO₄. *Phys. Rev. B* **2015**, *92*, 201112.
22. Brouet, V.; Mansart, J.; Perfetti, L.; Piovera, C.; Vobornik, I.; Le Fèvre, P.; Bertran, F.; Riggs, S. C.; Shapiro, M. C.; Giraldo-Gallo, P.; Fisher, I. R. Transfer of spectral weight across the gap of Sr₂IrO₄ induced by La doping. *Phys. Rev. B* **2015**, *92*, 081117.
23. Chikara, S.; Haskel, D.; Sim, J.-H.; Kim, H.-S.; Chen, C.-C.; Fabbris, G.; Veiga, L. S. I.; Souza-Neto, N. M.; Terzic, J.; Butrouna, K.; Cao, G.; Han, M. J.; van Veenendaal, M. Sr₂Ir_{1-x}Rh_xO₄ ($x < 0.5$): An inhomogeneous $j_{\text{eff}} = 1/2$ Hubbard system. *Phys. Rev. B* **2015**, *92*, 081114.
24. Haskel, D.; Fabbris, G.; Zhernenkov, M.; Kong, P. P.; Jin, C. Q.; Cao, G.; van Veenendaal, M. Pressure Tuning of the Spin-Orbit Coupled Ground State in Sr₂IrO₄. *Phys. Rev. Lett.* **2012**, *109*, 027204.
25. Chen, C.; Zhou, Y.; Chen, X.; Han, T.; An, C.; Zhou, Y.; Yuan, Y.; Zhang, B.; Wang, S.; Zhang, R.; Zhang, L.; Zhang, C.; Yang, Z.; DeLong, L. E.; Cao, G. Persistent insulating state at megabar pressures in strongly spin-orbit coupled Sr₂IrO₄. *Phys. Rev. B* **2020**, *101*, 144102.
26. Bhatti, I. N.; Rawat, R.; Banerjee, A.; Pramanik, A. K. Temperature evolution of magnetic and transport behavior in 5d Mott insulator Sr₂IrO₄: significance of magneto-structural coupling. *J. Phys.: Condens. Matter* **2014**, *27*, 016005.
27. Walker, D.; Carpenter, M. A.; Hitch, C. M. Some simplifications to multianvil devices for high pressure experiments. *Am. Mineral.* **1990**, *75*, 1020-1028.
28. Rodríguez-Carvajal, J. Recent advances in magnetic structure determination by neutron powder diffraction. *Physica B: Condensed Matter* **1993**, *192*, 55-69.
29. Dinnebier, R. E.; Billinge, S. J. L., Chapter 1 Principles of Powder Diffraction. In *Powder Diffraction: Theory and Practice*, The Royal Society of Chemistry: 2008; pp 1-19.

30. Sheldrick, G. Crystal structure refinement with SHELXL. *Acta Crystallogr., Sect. C* **2015**, *71*, 3-8.
31. Sheldrick, G. SHELXT - Integrated space-group and crystal-structure determination. *Acta Crystallogr., Sect. A* **2015**, *71*, 3-8.
32. Huang, Q.; Soubeyroux, J. L.; Chmaissem, O.; Sora, I. N.; Santoro, A.; Cava, R. J.; Krajewski, J. J.; Peck, W. F. Neutron Powder Diffraction Study of the Crystal Structures of Sr₂RuO₄ and Sr₂IrO₄ at Room Temperature and at 10 K. *J. Solid State Chem.* **1994**, *112*, 355-361.
33. Plotnikova, E. M.; Daghofer, M.; van den Brink, J.; Wohlfeld, K. Jahn-Teller Effect in Systems with Strong On-Site Spin-Orbit Coupling. *Phys. Rev. Lett.* **2016**, *116*, 106401.
34. Dikushina, E. A.; Avvakumov, I. L. Study of the influence of a spin-orbit exciton on the magnetic ordering in Sr₂IrO₄. *J. Phys. Conf. Ser.* **2016**, *741*, 012016.
35. Crawford, M. K.; Subramanian, M. A.; Harlow, R. L.; Fernandez-Baca, J. A.; Wang, Z. R.; Johnston, D. C. Structural and magnetic studies of Sr₂IrO₄. *Phys. Rev. B* **1994**, *49*, 9198-9201.
36. Samanta, K.; Tartaglia, R.; Kaneko, U. F.; Souza-Neto, N. M.; Granado, E. Anisotropic lattice compression and pressure-induced electronic phase transitions in Sr₂IrO₄. *Phys. Rev. B* **2020**, *101*, 075121.
37. Samanta, K.; Ardito, F. M.; Souza-Neto, N. M.; Granado, E. First-order structural transition and pressure-induced lattice/phonon anomalies in Sr₂IrO₄. *Phys. Rev. B* **2018**, *98*, 094101.
38. Longo, J. M.; Raccach, P. M. The structure of La₂CuO₄ and LaSrVO₄. *J. Solid State Chem.* **1973**, *6*, 526-531.
39. Ye, F.; Chi, S.; Chakoumakos, B. C.; Fernandez-Baca, J. A.; Qi, T.; Cao, G. Magnetic and crystal structures of Sr₂IrO₄: A neutron diffraction study. *Phys. Rev. B* **2013**, *87*, 140406.
40. Kini, N. S.; Strydom, A. M.; Jeevan, H. S.; Geibel, C.; Ramakrishnan, S. Transport and thermal properties of weakly ferromagnetic Sr₂IrO₄. *J. Phys.: Condens. Matter* **2006**, *18*, 8205-8216.
41. Pallecchi, I.; Buscaglia, M. T.; Buscaglia, V.; Gilioli, E.; Lamura, G.; Telesio, F.; Cimberle, M. R.; Marré, D. Thermoelectric behavior of Ruddlesden–Popper series iridates. *J. Phys.: Condens. Matter* **2016**, *28*, 065601.
42. Cao, G.; Bolivar, J.; McCall, S.; Crow, J. E.; Guertin, R. P. Weak ferromagnetism, metal-to-nonmetal transition, and negative differential resistivity in single-crystal Sr₂IrO₄. *Phys. Rev. B* **1998**, *57*, R11039-R11042.

Non-centrosymmetric Sr₂IrO₄ obtained under high pressure

Haozhe Wang^{1‡}, Madalynn Marshall^{2‡}, Zhen Wang³, Kemp W. Plumb⁴, Martha Greenblatt², Yimei Zhu³, David Walker⁵, Weiwei Xie^{1*}

1. Department of Chemistry, Michigan State University, East Lansing, Michigan 48824, USA
2. Department of Chemistry and Chemical Biology, Rutgers University, Piscataway, New Jersey 08854, USA
3. Condensed Matter Physics and Materials Science Department, Brookhaven National Laboratory, Upton, New York 11973, USA
4. Department of Physics, Brown University, Providence, Rhode Island 02912, USA
5. Lamont Doherty Earth Observatory, Columbia University, Palisades, New York 10964, USA

‡ H.W. and M.M. contributed equally. * Email: xieweiwe@msu.edu

Supporting Information

Table S1 Single crystal X-ray diffraction data at room temperature and 100 K.....	S2
Table S2 Anisotropic displacement parameters	S3
Table S3 Atomic coordinates and equivalent isotropic displacement parameters	S4
Figure S1 PXRD overlay of Sr ₂ IrO ₄	S5
Figure S2 Magnetic susceptibility and Curie-Weiss fitting.....	S6
Figure S3 Magnetic hysteresis	S7
Figure S4 Field dependence of specific heat	S8
Figure S5 Specific heat data fitted by Debye and Einstein model.....	S9
Figure S6 Low temperature specific heat data (2–20 K)	S10
Figure S7 Temperature dependence of resistivity.....	S11
Figure S8 Resistivity data fitted by Equation 9 with ν of 1/2 and 1/4	S12
Table S4 Summary of fitting parameters for resistivity data	S13

Table S1 Single crystal X-ray diffraction data at room temperature and 100 K.

Temperature	Room Temperature	100 K
Refined formula	Sr ₂ IrO ₄	Sr ₂ IrO ₄
FW (g/mol)	431.44	431.44
Space group	<i>I4mm</i>	<i>I4mm</i>
<i>a</i> (Å)	3.8860(5)	3.8777(5)
<i>c</i> (Å)	12.826(2)	12.825(2)
<i>V</i> (Å³)	193.69(6)	192.85(6)
Extinction Coefficient	N/A	N/A
θ range (°)	3.177–33.030	3.177–33.075
# of reflections; R_{int}	1088; 0.0627	1286; 0.0591
# of independent reflections	267	264
# of parameters	23	23
R_1; ωR_2 ($I > 2\delta(I)$)	0.0409; 0.0651	0.0312; 0.0443
Goodness of fit (GOF)	1.177	1.125
Diffraction peak and hole (e⁻/ Å³)	3.658, -3.492	2.359, -1.96

Table S2 Anisotropic displacement parameters for Sr₂IrO₄ at room temperature and 100 K.

Sr₂IrO₄ at Room Temperature						
Atom	U¹¹	U²²	U³³	U²³	U¹³	U¹²
Ir1	-0.0018(6)	-0.0018(6)	-0.0021(6)	0	0	0
Sr1	0.026(7)	0.026(7)	0.007(7)	0	0	0
Sr2	-0.001(4)	-0.001(4)	0.005(6)	0	0	0
O1	0.03(2)	0.03(2)	-0.02(2)	0	0	0
O2	-0.006(10)	-0.006(10)	-0.023(18)	0	0	0
O3	0.04(3)	0.003(11)	-0.01(3)	0	0.02(3)	0

Sr₂IrO₄ at 100 K						
Atom	U¹¹	U²²	U³³	U²³	U¹³	U¹²
Ir1	-0.0004(3)	-0.0004(3)	0.0012(7)	0	0	0
Sr1	0.005(8)	0.005(8)	0.005(4)	0	0	0
Sr2	0.002(8)	0.002(8)	0.000(4)	0	0	0
O1	0.005(8)	0.005(8)	-0.033(15)	0	0	0
O2	0.012(10)	0.012(10)	-0.033(14)	0	0	0
O3	0.009(10)	0.005(7)	0.006(8)	0	0.01(3)	0

Table S3 Atomic coordinates and equivalent isotropic displacement parameters for Sr₂IrO₄ at room temperature and 100 K. (U_{eq} is defined as one-third of the trace of the orthogonalized U_{ij} tensor (\AA^2)).

Sr₂IrO₄ at Room Temperature						
Atom	Wyck.	<i>x</i>	<i>y</i>	<i>z</i>	Occ.	U_{eq}
Ir1	<i>2a</i>	0	0	0.1513(13)	1	-0.0019(4)
Sr2	<i>2a</i>	0	0	0.5044(4)	1	0.020(4)
Sr1	<i>2a</i>	0	0	0.79985(2)	1	0.001(3)
O1	<i>2a</i>	0	0	0.328(4)	1	0.013(18)
O2	<i>2a</i>	0	0	0.000(4)	1	-0.011(7)
O3	<i>8d</i>	0.419(9)	0	0.661(7)	0.5	0.010(15)

Sr₂IrO₄ at 100 K						
Atom	Wyck.	<i>x</i>	<i>y</i>	<i>z</i>	Occ.	U_{eq}
Ir1	<i>2a</i>	0	0	0.1489(7)	1	0.0001(3)
Sr2	<i>2a</i>	0	0	0.5019(4)	1	0.005(5)
Sr1	<i>2a</i>	0	0	0.7978(2)	1	0.002(5)
O1	<i>2a</i>	0	0	0.321(3)	1	-0.008(6)
O2	<i>2a</i>	0	0	0.000(3)	1	-0.003(8)
O3	<i>8d</i>	0.412(4)	0	0.649(6)	0.5	0.007(4)

Figure S1 Powder X-ray diffraction pattern overlay. The experimental data of high pressure Sr_2IrO_4 phase synthesized at $1400\text{ }^\circ\text{C}$ for ~ 4 hrs (black line) and ~ 28 hrs (red line) were presented. Bragg peak positions are indicated as Sr_2IrO_4 and $\text{Sr}_3\text{Ir}_2\text{O}_7$ with green and purple vertical tick marks, respectively.

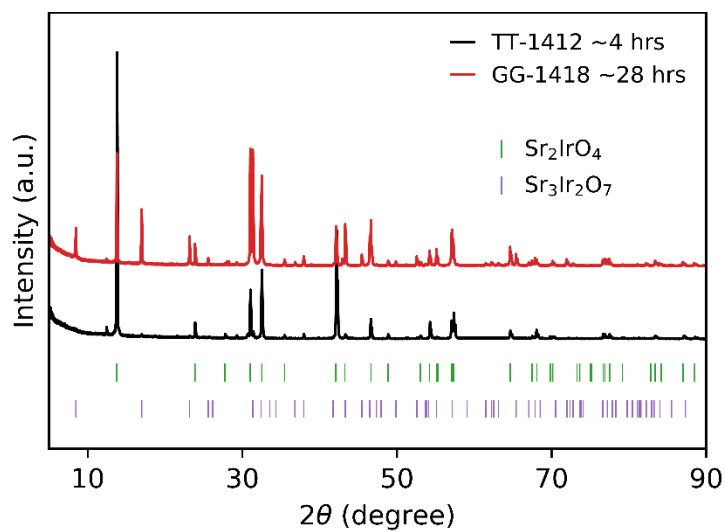


Figure S2 Magnetic susceptibility and Curie-Weiss fitting. (a) Temperature derivative of magnetic susceptibility χ at 1000 Oe under FCW mode. The minimum at around 84 K was highlighted by red circle and an arrow. (b) The inverse magnetic susceptibility data (FCW, 80–140 K, blue hollow circle) fitted with the modified Curie-Weiss model (orange line). (c) The Curie-Weiss fit was further extrapolated to 160 K.

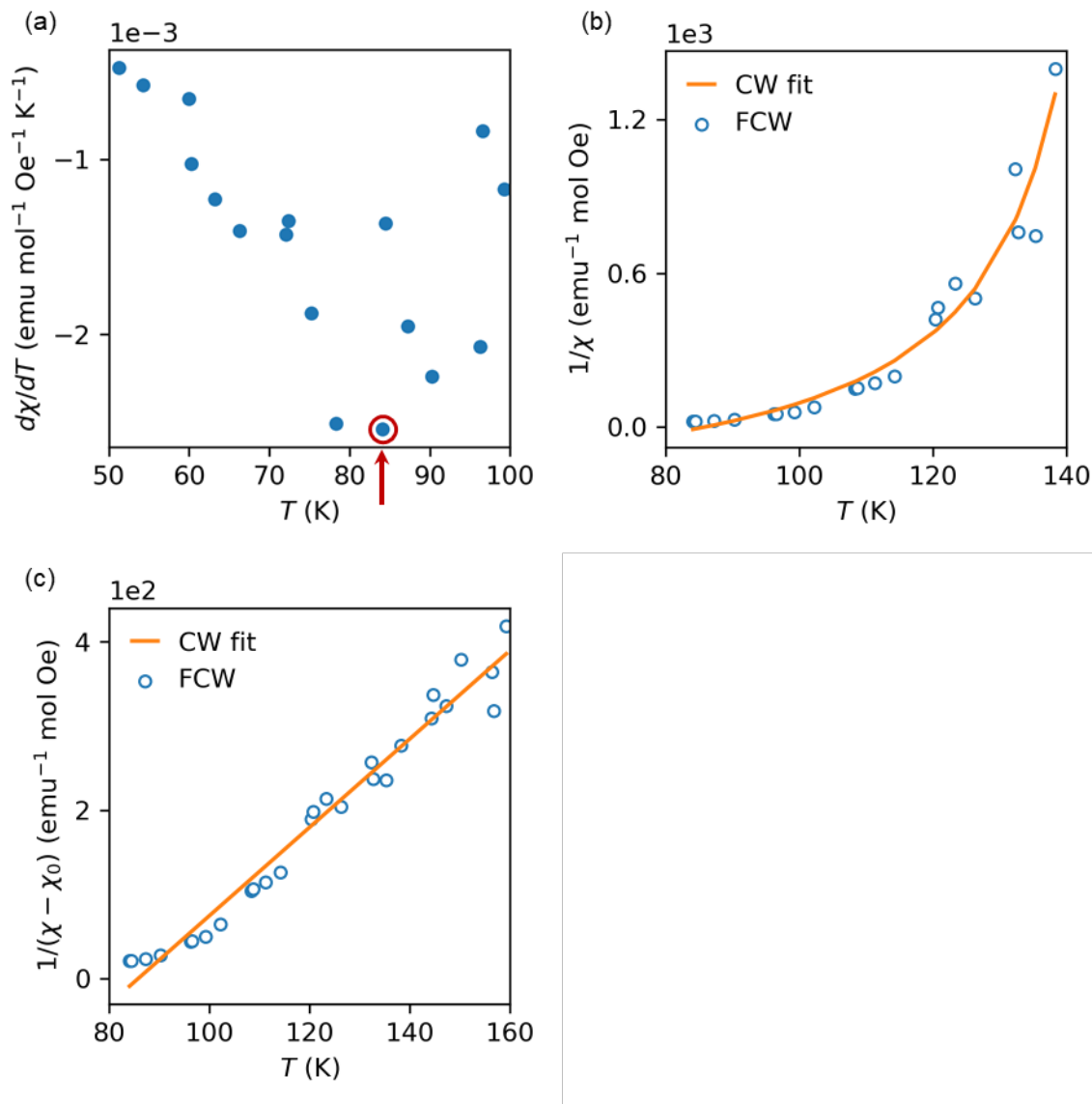


Figure S3 Magnetic hysteresis. Magnetic hysteresis observed in the high pressure Sr_2IrO_4 phase at 2 K ranging from -0.6 T to 0.6 T.

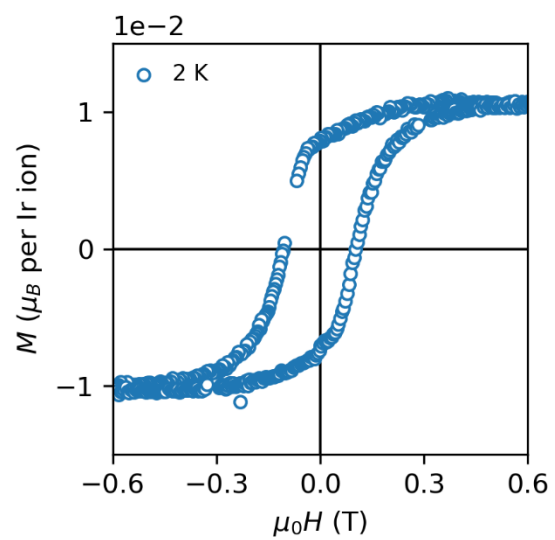


Figure S4 Field dependence of specific heat. Temperature dependence of specific heat data over temperature (C_p/T) for high pressure Sr_2IrO_4 phase, under 0 T (blue), 0.05 T (orange), and 1 T (green). No significant differences were observed. No λ shape anomalies emerged in the whole temperature regime studied under either case.

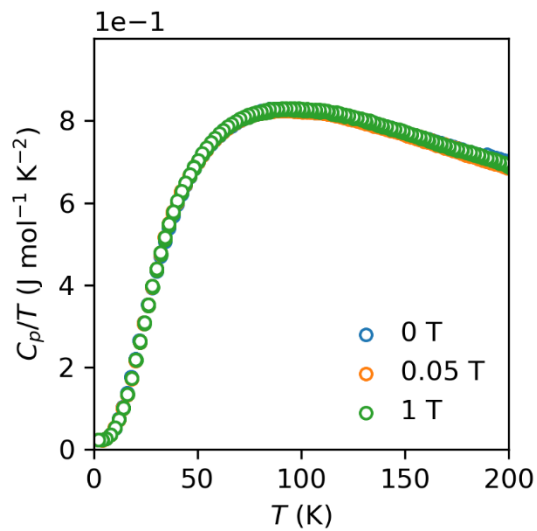


Figure S5 Specific heat data fitted by Debye and Einstein model. Temperature dependence of specific heat data over temperature under 0 T (C_p/T , blue hollow circle) for high pressure Sr_2IrO_4 phase, fitted by (a) Debye model, (b) Einstein model, (c) two Debye model with the electronic contribution included, and weighted Debye model (d) without and (e) with the electronic contribution included.

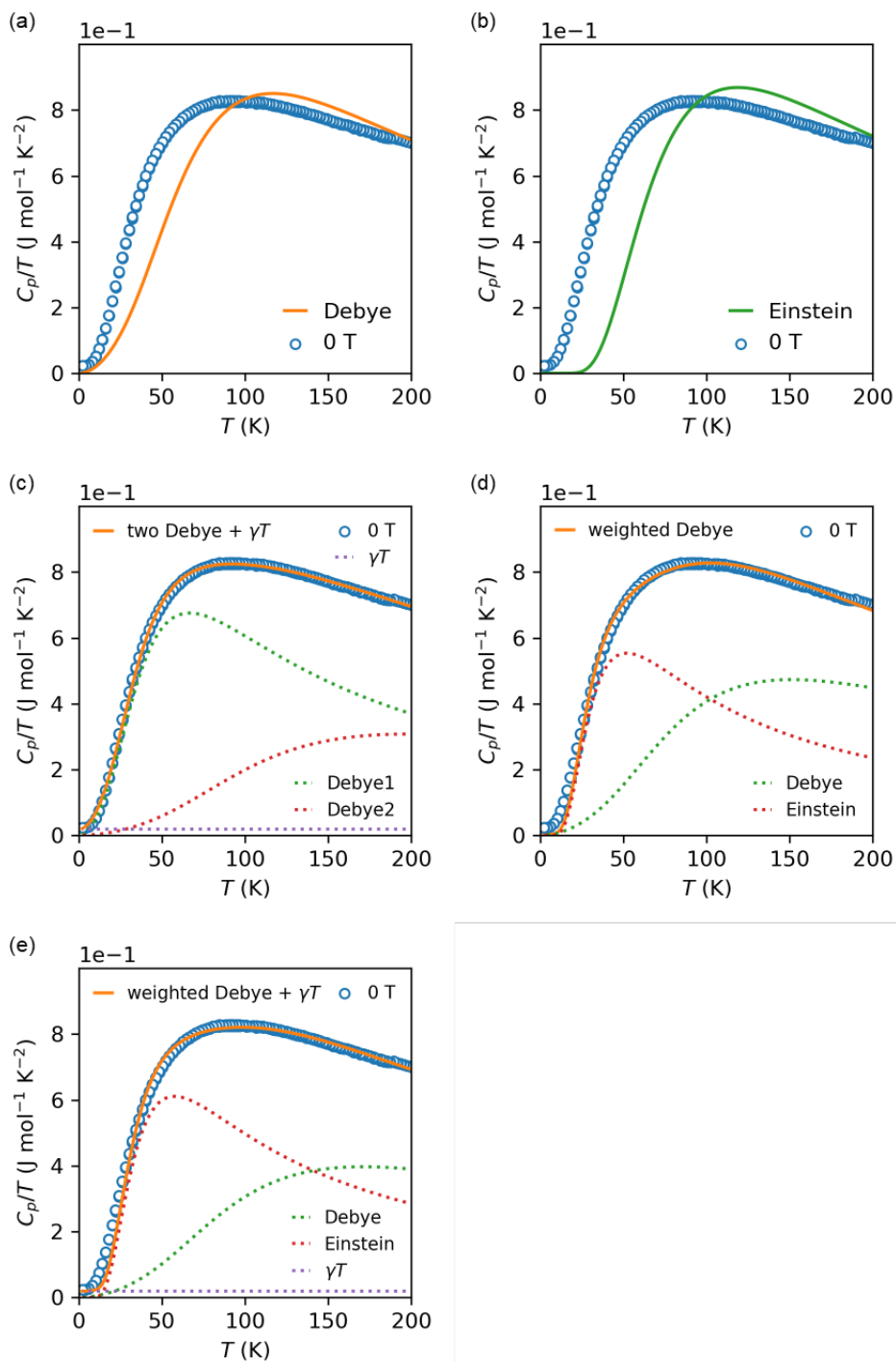


Figure S6 Low temperature specific heat data (2–20 K). Specific heat data over temperature (C_p/T) plotted versus T^2 under low temperature regime, 2–20 K, providing the possibility to derivate the Sommerfeld parameter, γ .

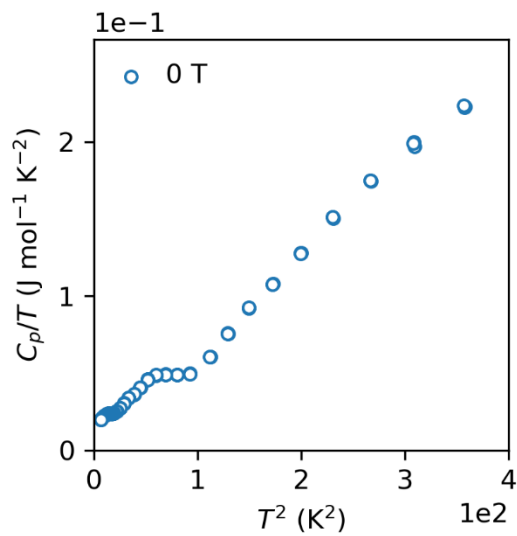


Figure S7 Temperature dependence of resistivity. Temperature dependence of the resistivity data ρ plotted as $\ln \rho$ versus (a) T^{-1} , (b) $T^{-1/2}$, and (c) $T^{-1/4}$ under 0 T.

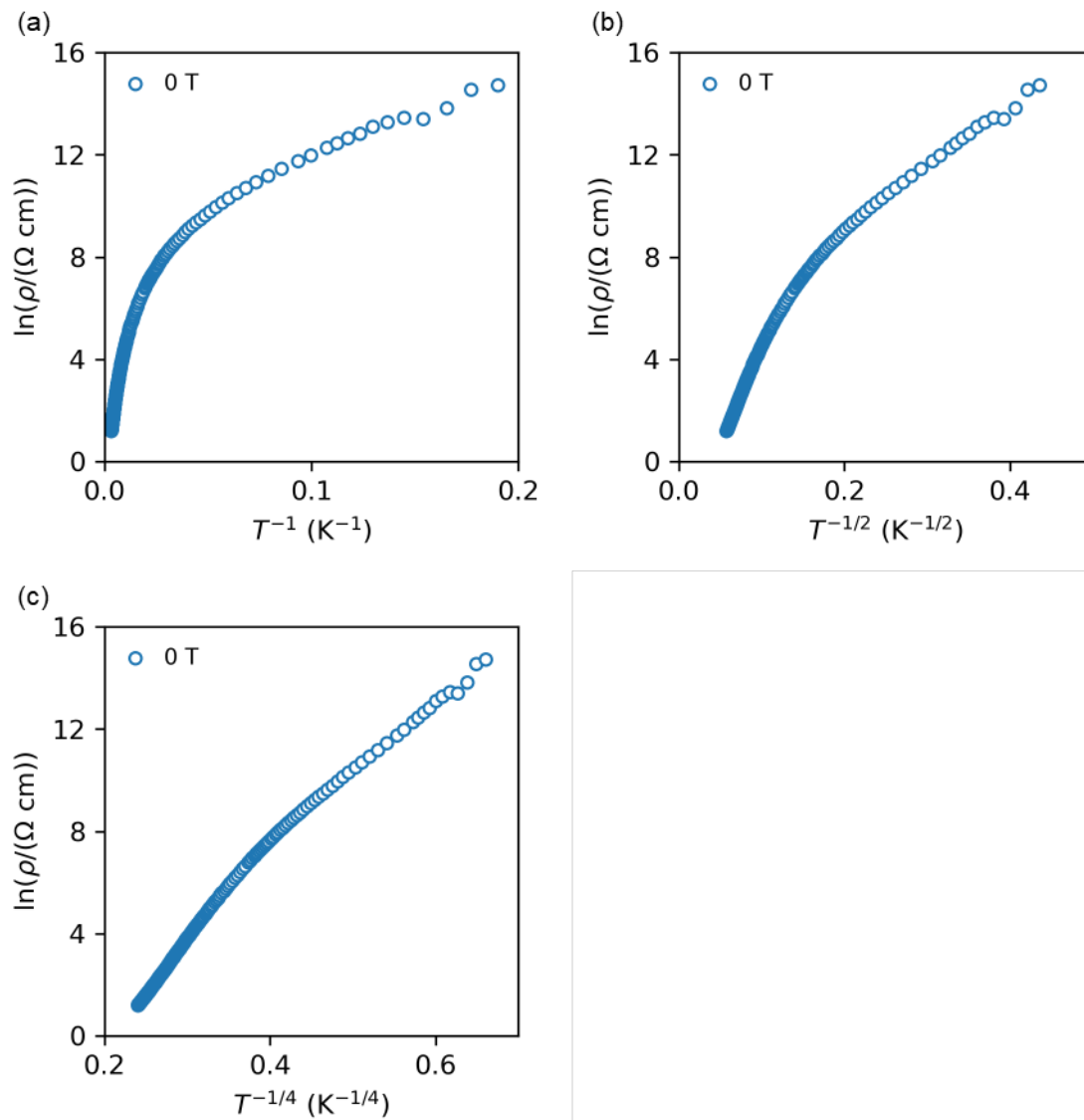


Figure S8 Resistivity data fitted by Equation 9 with ν of 1/2 and 1/4. (a) The resistivity data ρ (blue hollow circle) ranging from 110–300 K fitted by **Equation 9** with ν of 1/2 (orange line). (b) The resistivity data ρ in the low temperature regime ranging from 8–20 K fitted by **Equation 9** with ν of 1/2. (c) The resistivity data ρ in the low temperature regime ranging from 10–20 K fitted by **Equation 9** with ν of 1/4. Fitting parameters were summarized in **Table S4**. The value ν of 1/4 is favored over 1/2.

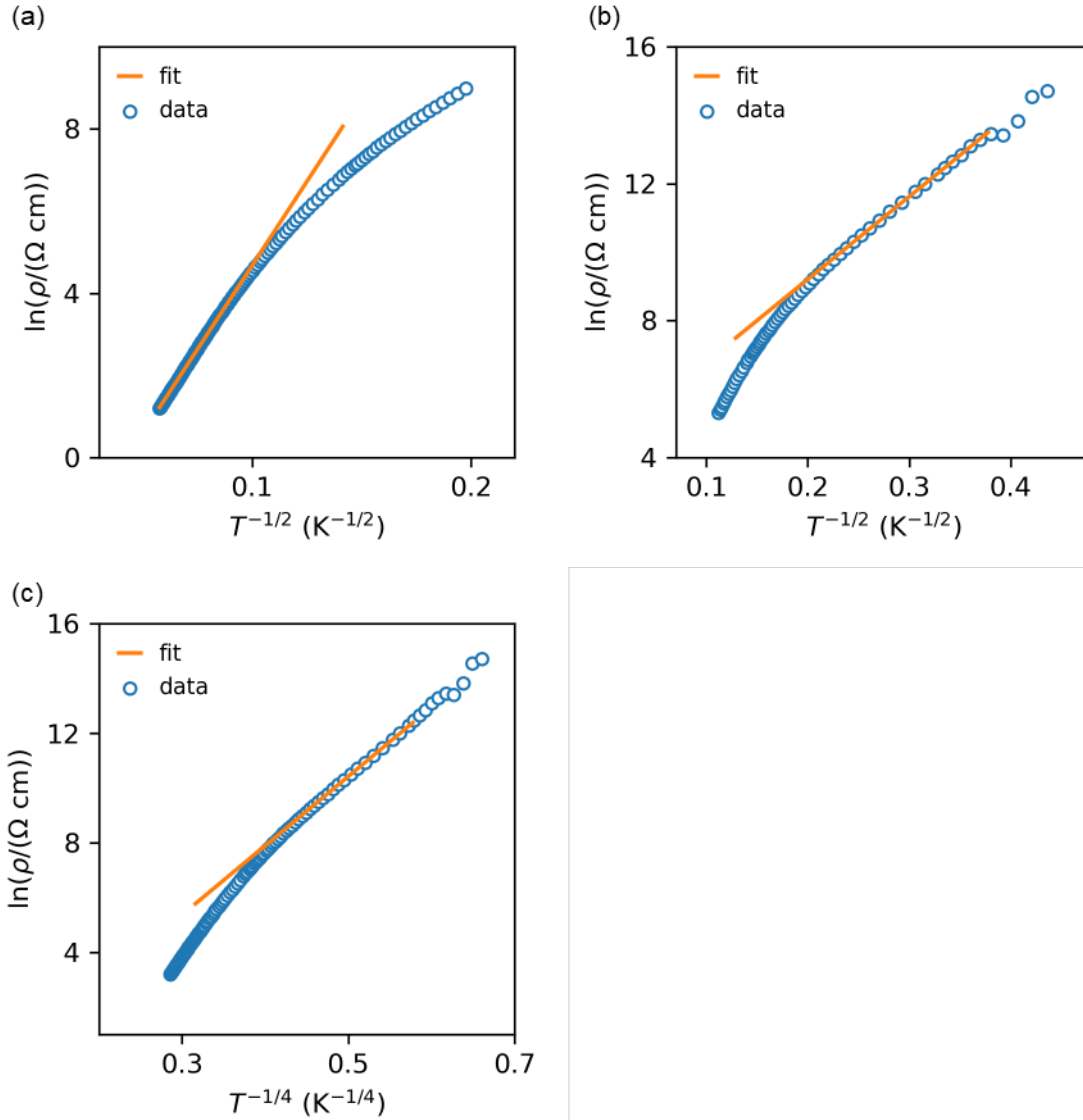


Table S4. Summary of fitting parameters for resistivity data. Summary of fitting parameters for the resistivity data ρ by **Equation 9**. R^2 is the coefficient of determination.

$\nu = 1/2$			
Temperature Range / K	$\rho_0 / (\Omega \text{ cm})$	T_0 / K	R^2
110–300	$3.01(4) \times 10^{-5}$	6682	0.9996
8–20	79.6(37)	583	0.9996
$\nu = 1/4$			
Temperature Range / K	$\rho_0 / (\Omega \text{ cm})$	T_0 / K	R^2
80–300	$7.82(12) \times 10^{-5}$	3.83×10^6	0.9998
10–20	-2.23(4)	4.10×10^5	0.9999